The Polar Structures of $KNdNb_2O_7$ and $KNdTa_2O_7$.

Subhadip Mallick[†], Alexandra S. Gibbs[‡], Weiguo Zhang[§], P. Shiv Halasyamani[§], Nicole A. Benedek[¶]*, and Michael A. Hayward[†]*

[†] Department of Chemistry, University of Oxford, Inorganic Chemistry Laboratory, South Parks Road, Oxford, OX1 3QR, UK.

[¶] Department of Materials Science and Engineering, Cornell University, Ithaca, New York 14853, USA.

[‡] ISIS Facility, Rutherford Appleton Laboratory, Chilton, Oxon OX11 0QX, UK.

[§] Department of Chemistry, University of Houston, 112 Fleming Building, Houston, Texas 77204-5003, USA.

ABSTRACT: Na-for-Rb cation exchange followed by K-for-Na cation exchange of $RbNdM_2O_7$ (*M* = Nb, Ta) yields the corresponding, metastable $KNdM_2O_7$ phases. Synchrotron X-ray and neutron powder diffraction data, combined with powder SHG data, reveal that the $KNdM_2O_7$ phases adopt a polar structure (space group *Im*2*m*) consisting of NdM_2O_7 double perovskite sheets stacked in a (0, ½, *z*) manner with K^+ cations ordered within the 6-coordinate prismatic inter-layer sites. The perovskite double sheets adopt an ($a^0b^+c^0/a^0$-b^+c^0) tilting distortion, however unlike other *A*'AB_2O_7 phases this distortion is not the origin of the non-centrosymmetric structure, which is attributed to a second-order Jahn-Teller distortion of the MO_6 units. First-principles DFT calculations confirm the polar *Im*2*m* phase is more stable than the corresponding centrosymmetric alternative. The role of the *A*'- and *A*- cations in directing the stacking patterns and tilting distortions of *A*'AB_2O_7 phases is discussed with reference to hybrid improper ferroelectric behavior.

Introduction

Ferroelectric materials are widely used in technology due to their spontaneous and switchable electrical polarizations.[1] However, the discovery of new ferroelectric materials is challenging because a non-centrosymmetric (NCS) crystal structure is a prerequisite for a spontaneous electrical polarization,[2-3] but acentric crystal structures tend to be energetically disfavored compared to centrosymmetric alternatives.

A common method of favoring an NCS crystal structure is to utilize a second-order Jahn-Teller distortion (SOJT) to break the inversion symmetry of a material. For example, inclusion of an octahedrally coordinated, d^0 transition-metal ion (e.g. Ti^{4+} in $BaTiO_3$)[4-7] or a post-transition metal with an ns^2 electronic configuration (e.g. Pb^{2+} in $PbTiO_3$)[8-13] can break local inversion symmetry, driven by the mixing of empty cation and filled anion orbital states. However, the necessity to include such metal cations limits which elements can be included in NCS materials, and hampers attempts to combine ferroelectricity with magnetism, in the search for magnetoelectric multiferroic materials.[14]

An alternative method of preparing NCS phases utilizes a 'trilinear coupled hybrid improper' mechanism.[15] This mechanism utilizes the low-energy tilting and twisting distortions of the BO_6 units in ABO_3 perovskite phases, by exploiting the observation that suitable combinations of these tilting distortions can combine such that two non-polar distortion modes couple to a third, polar distortion mode (trilinear coupling) yielding an NCS structure.[15-17] As these distortion modes impose no chemical requirements, the trilinear coupled hybrid improper mechanism offers the prospect of broadening the chemical diversity of ferroelectric materials.

The reciprocal nature of the collective BO_6 rotations in 3D perovskite frameworks means that in addition to the correct tilting distortions, *A*- or *B*-cation order is required to break the global (rather than just local) inversion symmetry of an ABO_3 perovskite phase [18] – a restriction that poses significant synthetic challenges.[19-20] However, this requirement does not apply to layered variants of the perovskite structure, so much attention has been focused on applying trilinear coupling to compounds with these structure types.[21]

Initially both computational and experimental effort was focused on the $A_3B_2O_7$, *n* = 2 Ruddlesden-Popper phases, which consist of AB_2O_7 perovskite double-layers, stacked in a (½, ½, *z*) arrangement, separated by 9-coordinate *A*-cations, as shown in Figure 1. Theory predictions of trilinear coupled ferroelectric behavior [15] have been experimentally verified in a number of Ruddlesden-Popper phases, including (Ca, Sr)Ti_2O_7, $Sr_3Zr_2O_7$, (Sr, Ca)Sn_2O_7 and $Ca_3Mn_2O_7$.[22-25]

Trilinearly-coupled ferroelectric behavior has also been predicted for *A*'AB_2O_7 *n* = 2 Dion-Jacobson phases,[26] in which the AB_2O_7 perovskite layers are stacked in a (0, 0, *z*) arrangement, separated by large 8-coordinate *A*'-cations, as shown in Figure 1. Combined experimental and computational studies have confirmed that Dion-Jacobson phases such as $CsNdM_2O_7$ and $RbNdM_2O_7$ (*M* = Nb, Ta) adopt polar structures due to trilinear coupling,[27-28] although ferroelectric switching is yet to be demonstrated for these materials.

The *A*'-cations in Dion-Jacobson phases exhibit a range of facile cation-exchange reactions.[29-31] If large cations such as Cs^+ or Rb^+ are exchanged for smaller cations, such as Na^+ or Li^+, the resulting *A*'AB_2O_7 phases adopt Ruddlesden-Popper structures, with the change from a (0, 0, *z*) to a (½, ½, *z*) stacking of the AB_2O_7 perovskite sheets motivated by the formation of 4-coordinate, pseudo tetrahedral sites to accommodate the small *A*'-cations (Figure 1).[32-35] However, if K^+ cations are substituted into the *A*'-cation sites, the resulting KAB_2O_7 compounds adopt layered perovskite structures in which the AB_2O_7 layers stack in a (0, ½, *z*) arrangement with the K^+ cations accommodated within 6-coordinate trigonal prismatic sites (Figure 1).[32, 36-37]

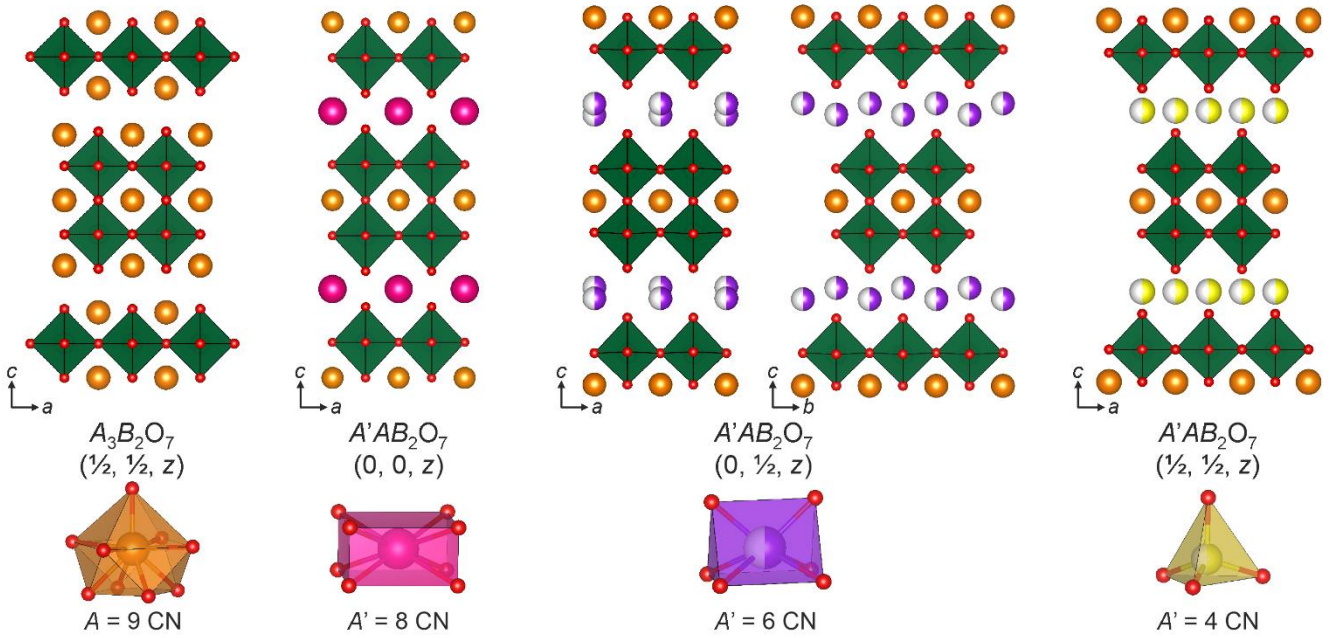

Figure 1. The structures of the aristotype $n = 2$ layered perovskite phases and the coordination polyhedra of the *A*- and *A*'-cations that reside between the perovskite double-sheets. Half-shading of the 4-CN and 6-CN *A*'-cation sites indicates a disordered 50% occupancy.

Here we report the detailed structural characterization of $KNdTa_2O_7$ and $KNdNb_2O_7$, synthesized from the corresponding $RbNdM_2O_7$ phases using low-temperature cation exchange reactions. Both potassium compounds adopt polar structures at room temperature, which do not appear to be stabilized by the trilinear coupling mechanism. Instead their polar structures are attributed to an SOJT distortion of the $Nb^{5+}O_6$ and $Ta^{5+}O_6$ polyhedra, suggesting that these two stability mechanisms are often in competition in layered perovskite oxides.

Experimental

Synthesis. Samples of $KNdNb_2O_7$ and $KNdTa_2O_7$ were prepared by first synthesizing the corresponding $RbNdM_2O_7$ (*M* = Nb, Ta) phases,[27] then converting them to the corresponding $NaNdM_2O_7$ phases via Na-for-Rb cation exchange,[38] and finally converting them to the $KNdM_2O_7$ phases via K-for-Na cation exchange.

Specifically, samples of $RbNdNb_2O_7$ and $RbNdTa_2O_7$ were prepared from Rb_2CO_3 (99.8%), Nd_2O_3 (99.99%, dried at 900 ºC) and Nb_2O_5 (99.9985%, dried at 900 ºC) or Ta_2O_5 (99.993%, dried at 900 ºC) as described previously.[27] Suitable stoichiometric ratios of the oxides were ground together in an agate pestle and mortar and then combined with a 50% excess of Rb_2CO_3 (to compensate for metal loss due to volatility at high temperature). These mixtures were then heated at 850 °C in air for 12 h, reground, and pressed into pellets. Samples of $RbNdNb_2O_7$ were heated in air for four periods of 48 h at 1000 °C and a further 48 h at 1050 °C. Samples of $RbNdTa_2O_7$ were heated in air for four periods of 48 h at 1050 °C. All samples were reground and pressed into pellets between heating cycles. After heating, all samples were washed with distilled water to remove any remaining excess rubidium oxide, and then dried for 12 h at 140 °C in air.

Sodium cation-exchange reactions were performed by reacting $RbNdNb_2O_7$ and $RbNdTa_2O_7$ with 10 mole-equivalents of $NaNO_3$ (>99.0%) as described previously.[38] These mixtures were ground together and loaded into an open ended silica tube and heated in air for two periods of 48 h at 400 °C. Between heating cycles, samples were washed with distilled water, dried for 12 h at 140 °C in air and mixed with a further 10 mole-equivalents of $NaNO_3$. After the final heating step, all samples were washed with distilled water to remove the $NaNO_3$ and then dried for 12 h at 140 °C in air.

Potassium cation-exchange reactions were performed by reacting $NaNdNb_2O_7$ and $NaNdTa_2O_7$ with 10 mole-equivalents of KNO_3 (99.995%). These mixtures were ground together and loaded into an open ended silica tube and heated in air for two periods of 48 h at 370 °C. Between heating cycles, samples were washed with distilled water, dried for 12 h at 110 °C in air and mixed with a further 10 mole-equivalents of KNO_3. After the final heating step, all samples were washed with distilled water to remove remaining $NaNO_3$ and then dried for 12 h at 110 °C in air.

Characterization. X-ray powder diffraction data were collected using a PANalytical X'pert diffractometer incorporating an X'celerator position-sensitive detector (monochromatic Cu $K\alpha_1$ radiation). High-resolution synchrotron X-ray powder diffraction (SXRD) data were collected using the I11 instrument at the Diamond Light Source Ltd. Diffraction patterns were collected using Si-calibrated X-rays with an approximate wavelength of 0.825 Å from samples, sealed in 0.3 mm diameter borosilicate glass capillaries. Time of flight neutron powder diffraction (NPD) data were collected using HRPD diffractometer at the ISIS neutron source from the samples loaded in 8 mm vanadium cans. Rietveld refinements were performed using the GSAS suite of programs.[39] The powder second harmonic generation (SHG) response of samples was recorded and compared to a standard sample of α-SiO_2. No index matching fluid was used in any of the experiments. A detailed description of the experimental setup and process has been reported previously.[40]

First-Principles Calculations. First-principles density functional theory (DFT) calculations were performed using the Vienna Ab Initio Simulation Package (VASP).[41-44] The PBEsol exchange-correlation functional [45] and projector-augmented wave pseudopotentials [46-47] were used for all calculations. The

valence electron configurations for each pseudopotential were as follows: $3s^2 3p^6 4s^1$ for K, $5s^2 5p^6 4d^4 5s^1$ for Nb, $5s^2 5p^6 4f^1 6s^2$ for Nd (three f-electrons frozen in the core), and $2s^2 2p^4$ for O. Structural relaxations were considered converged when the force on each atom became smaller than 1 meV/Å. All calculations were performed with a 700 eV plane wave cutoff and a 6×6×3 **k**-point mesh. Crystallographic analyses were performed with the aid of the ISOTROPY suite of programs [48] and the Bilbao Crystallographic Server.[49-50]

Results

Cation exchange route to synthesize KNdM_2O_7 phases. While the high-temperature solid-state synthesis of $KLaNb_2O_7$ has been reported [32, 37] the analogous neodymium phase is not accessible by direct heating of K_2CO_3, Nd_2O_3 and Nb_2O_5. When this combination of reagents is heated at 1100 °C the major product obtained is $NdNbO_4$, indicating that $KNdNb_2O_7$ is not the thermodynamically most stable product of these reagents, and so cannot be prepared by their direct combination at high temperature. Therefore, we have synthesized the metastable potassium phases $KNdNb_2O_7$ and $KNdTa_2O_7$ by a two-step cation exchange route starting from the corresponding $RbNdM_2O_7$ Dion-Jacobson phases and proceeding via the $NaNdM_2O_7$ Ruddlesden-Popper phases.

Structural Characterization of $KNdTa_2O_7$ and $KNdNb_2O_7$. High-resolution synchrotron X-ray and neutron powder diffraction data collected from $KNdTa_2O_7$ and $KNdNb_2O_7$ could initially be indexed using the unit cell reported for $KLaNb_2O_7$ [36] and previously reported for $KNdNb_2O_7$.[34] However, close inspection of diffraction data revealed a series of small peaks which can only be indexed using an $a' = 2 \times a$, $b' = b$, $c' = c$ geometric expansion of the aristotype unit cell ($KNdTa_2O_7$: a = 7.702 Å, b = 3.862 Å, c = 21.772 Å; $KNdNb_2O_7$: a = 7.709 Å, b = 3.871 Å, c = 21.556 Å) as shown in Figure S1.

Deducing the subtle structural distortions of layered perovskite phases from diffraction data can be challenging. To assist this process we have performed a symmetry analysis using the ISODISTORT software [51] to produce a list of 'chemically plausible' distortions of the n = 2 (0, ½, z) stacked framework, listed in Table S1 in the Supporting Information. We define 'chemically plausible' distortions as those which retain the equivalence of the BO_6 octahedra, and our initial assumption was that $KNdNb_2O_7$ and $KNdTa_2O_7$ adopt structures on this list. Considering these assumptions, we observe that only two distortions, *Ammm* (Glazer tilt $a^0b^+c^0/a^0b^+c^0$)[52-53] and *Immm* (Glazer tilt $a^0b^+c^0/a^0\text{-}b^+c^0$) are consistent with the observed lattice parameters of the $KNdM_2O_7$ phases. However, further examination of the NPD data allows us to eliminate the *Ammm* space group based on extinction conditions as shown in Figures S2 and S3 in the Supporting Information.

A structural model was constructed based on the *Immm* ($a^0b^+c^0/a^0\text{-}b^+c^0$) distortion. In this structure there are two independent trigonal prismatic crystallographic sites (4*i* and 4*j*) on which to locate 4 potassium cations. As a result, the potassium cations can either be ordered on one or other of these sites or disordered across both of them. Potassium disordered structural models were constructed for $KNdNb_2O_7$ and $KNdTa_2O_7$ and in both cases, when refined against NPD data, the occupancy of the 4*i* site approached unity, while that of the 4*j* site approached zero. Thus, models with the potassium ions ordered on the 4*i* sites were constructed for $KNdNb_2O_7$ and $KNdTa_2O_7$ and refined against the NPD data to give reasonable fits to the data, as described in Table 1.

Space group	χ^2	R_p (%)	$_wR_p$ (%)	Number of variables
$KNdTa_2O_7$				
Immm	35.59	6.09	6.67	67
*Im*2*m*	28.26	5.50	5.94	77
*I*222	34.99	6.04	6.61	70
$KNdNb_2O_7$				
Immm	48.91	7.17	7.52	69
*Im*2*m*	38.88	6.61	6.70	77
*I*222	44.74	6.63	7.19	72

Table 1. Fitting statistics for the structural refinement of $KNdTa_2O_7$ and $KNdNb_2O_7$ against neutron powder diffraction data.

SHG data collected from $KNdTa_2O_7$ and $KNdNb_2O_7$ indicate that both compounds are SHG active (0.5 and 0.56 times α–SiO_2 respectively, compared to a minimum sensitivity of 5% of the α–SiO_2 signal) and thus adopt non-centrosymmetric crystal structures, so the *Immm* symmetry models cannot be correct. Given that none of the distortions in Table S1 are non-centrosymmetric, and noting the good fit achieved by the *Immm* ($a^0b^+c^0/a^0\text{-}b^+c^0$) distorted model, non-centrosymmetric structures based on a further distortion of this *Immm* model were constructed, again using the ISODISTORT software.[51] This analysis revealed two candidate non-centrosymmetric structures, described in the space groups *Im*2*m* and *I*222, which are generated by applying the Γ_4^- and Γ_1^- irreducible representations of the *Immm* space group respectively to the centrosymmetric *Immm* model. Refinement of the structural models described in space groups *Im*2*m* and *I*222 against the NPD data proceeded smoothly. A visual comparison of the fits to the data by the different models (Figure S4 and S5, Supporting Information), and the fitting statistics listed in Table 1, indicate that the *Im*2*m* model gives a marginally better fit to the data than either the centrosymmetric *Immm* model or the non-centrosymmetric *I*222 model.

Close inspection of the different refined structures of $KNdNb_2O_7$ and $KNdTa_2O_7$ provides further confirmation that the *Im*2*m* structural model is the best description of these phases. As shown in Tables 2 and 3, lowering the symmetry from *Immm* to *I*222 lowers the site symmetry of the Nb/Ta position from 8*m* to 8*k*, allowing the *y*-coordinate of this site to take a non-zero value. However, it can be seen that in the refined *I*222 models the Nb/Ta cations remain at y = 0, within error, thus the atomic configuration of the *I*222 models remains centrosymmetric, within error. In contrast lowering the symmetry to *Im*2*m* allows all 4 crystallographically distinct cation sites to adopt non-zero *y*-coordinates, and as can be seen in Tables 2 and 3, in the refined *Im*2*m* structures all 4 cations displace from y = 0 by amounts significantly greater than the error bounds, providing further validation of the *Im*2*m* models.

A complete description of the refined structures of $KNdTa_2O_7$ and $KNdNb_2O_7$ are given in Tables S2 and S4 respectively with selected bond lengths in Tables S3 and S5 respectively in the Supporting Information. Observed and calculated data plotted in Figure 2, and a representation of the refined structure of $KNdNb_2O_7$ shown in Figure 3.

Atom	Site	x	y	z	BVS
Immm					
K	4*i*	0	0	0.2334(4)	0.943
Nd(1)	2*a*	0	0	0	2.923
Nd(2)	2*b*	0.5	0	0	2.585
Ta	8*m*	0.7541(5)	0	0.3991(1)	5.522
*Im*2*m*					
K	4*c*	0	0.0074(37)	0.2354(4)	0.973
Nd(1)	2*a*	0	0.0182(36)	0	3.023
Nd(2)	2*b*	0.5	0.0405(27)	0	2.672
Ta	8*e*	0.7516(5)	0.0194(11)	0.3992(1)	5.293
*I*222					
K	4*i*	0	0	0.2325(5)	0.956
Nd(1)	2*a*	0	0	0	2.907
Nd(2)	2*b*	0.5	0	0	2.602
Ta	8k	0.7543(5)	0.0008(18)	0.3991(1)	5.540

Table 2. Fractional co-ordinates and cation bond valence sums from the structural refinement of $KNdTa_2O_7$ against powder neutron diffraction data.

Atom	Site	x	y	z	BVS
Immm					
K	4*i*	0	0	0.2358(4)	0.961
Nd(1)	2*a*	0	0	0	2.584
Nd(2)	2*b*	0.5	0	0	2.924
Nb	8*m*	0.7505(5)	0	0.3987(1)	5.397
*Im*2*m*					
K	4*c*	0	0.0078(38)	0.2371(4)	0.972
Nd(1)	2*a*	0	0.0123(29)	0	2.894
Nd(2)	2*b*	0.5	0.0113(25)	0	2.996
Nb	8*e*	0.7515(5)	0.0230(10)	0.3985(1)	5.324
*I*222					
K	4*i*	0	0	0.2362(4)	0.973
Nd(1)	2*a*	0	0	0	2.642
Nd(2)	2*b*	0.5	0	0	2.849
Nb	8*k*	0.7512(5)	0.9983(15)	0.3986(1)	5.402

Table 3. Fractional co-ordinates and cation bond valence sums from the structural refinement of $KNdNb_2O_7$ against powder neutron diffraction data.

We also performed first-principles DFT calculations on the *Immm*, *Im*2*m* and *I*222 phases of $KNdNb_2O_7$ to determine which was lowest in energy. Structural relaxation of $KNdNb_2O_7$ in *I*222 symmetry resulted in a structure with *Immm* symmetry. The Γ_1^- distortion, which connects the *Immm* and *I*222 phases, was essentially `pushed out' of the structure during the relaxation, suggesting that the *I*222 phase is not favored by our DFT calculations. We found the *Im*2*m* phase to be very marginally more stable than *Immm*, however the energy difference between the two phases is very small (< 1 meV/formula unit). The lattice parameters and atomic coordinates of $KNdNb_2O_7$ in *Im*2*m* are shown in Table S6 and are in excellent agreement with those determined experimentally.

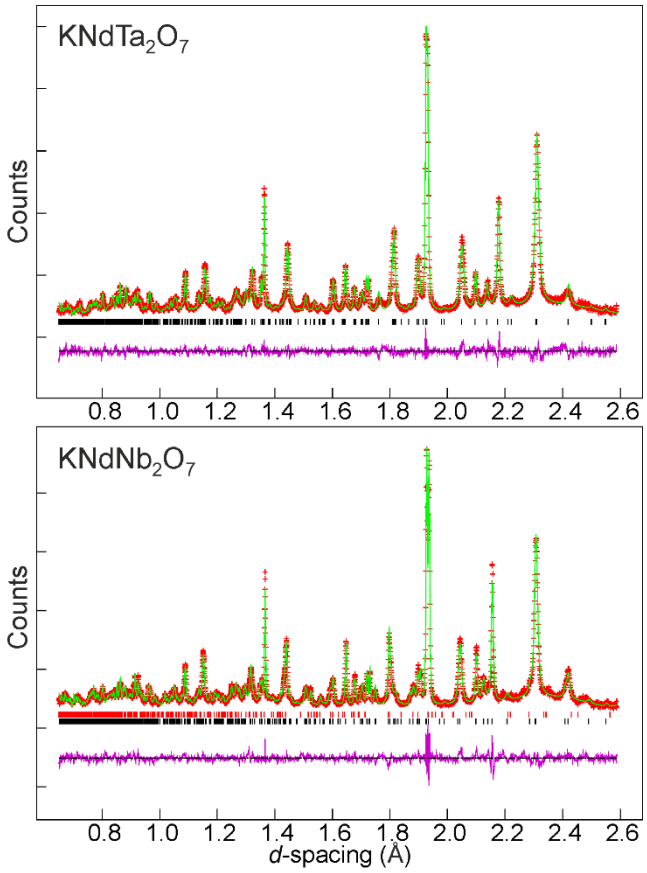

Figure 2. Observed calculated and difference plots from the structural refinement of $KNdTa_2O_7$ (top) and $KNdNb_2O_7$ (bottom) against neutron powder diffraction data collected at room temperature using the detector bank cantered around 168 °. Black tick marks indicate peak position for the majority phase, red tick marks (bottom panel only) for an $NdNbO_4$ secondary phase.

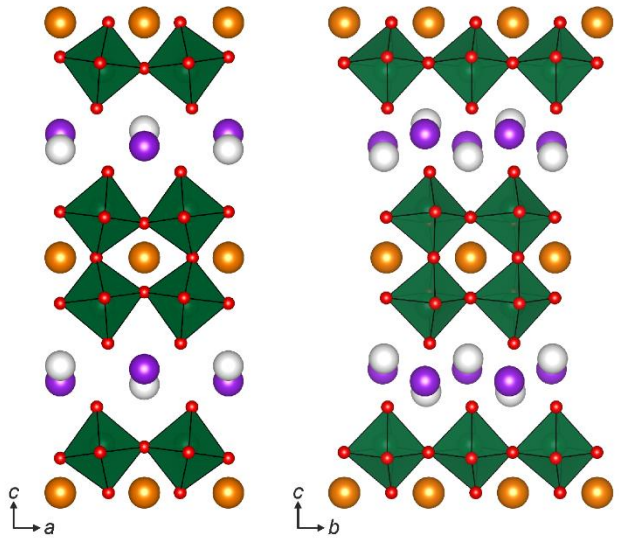

Figure 3. The $a^0b^+c^0/a^0\text{-}b^+c^0$ distorted structure of $KNdNb_2O_7$. Green, orange, red, purple and grey spheres represent Nb, Nd, O, K and K-vacancies respectively.

Discussion

The synthesis of $KNdTa_2O_7$ *via* the K-for-Rb cation exchange of $RbNdTa_2O_7$, has been reported previously.[34] In this work we have confirmed that this conversion is facile, as is the 2-step route $RbNdTa_2O_7 \rightarrow LiNdTa_2O_7 \rightarrow KNdTa_2O_7$ using sequential Li-for-Rb and K-for-Li cation exchange. However, to prepare the $KNdM_2O_7$ (M = Nb, Ta) compounds in this study we have used the 2-step process: $RbNdM_2O_7 \rightarrow NaNdM_2O_7 \rightarrow KNdM_2O_7$ using sequential Na-for-Rb and K-for-Na cation exchange. This is because we wanted to ensure that the observed SHG activity of the $KNdM_2O_7$ phases was not due to the presence of small quantities of the non-centrosymmetric compounds $RbNdM_2O_7$ and/or $LiNdM_2O_7$ due to incomplete cation-exchange, so we utilized a route via the centrosymmetric $NaNdM_2O_7$ intermediates.

The polar structures of $KNdTa_2O_7$ and $KNdNb_2O_7$ can be derived from the aristotype n = 2 (0, ½, z) structure (space group *Ammm* #65) by the sequential application of two distortion modes, the Γ_1^+ mode which adds an $a^0b^+c^0/a^0$-b^+c^0 cooperative tilting distortion of the MO_6 octahedra, and a Γ_4^- polar distortion. Considering the tilting distortion first, we note that the collective tilting and twisting distortions of ABO_3 perovskite phases, and related layered analogues, occur in response to a size mismatch between the *A*- and *B*-cations, because the rotation of the BO_6 units can shorten the average *A*-O bond length without changing the average *B*-O bond length. For the 3D ABO_3 perovskite structure the magnitude of the size-mismatch between *A*- and *B*-cations can be evaluated using the structural tolerance factor, $t = \langle A\text{-O}\rangle/(\sqrt{2}\langle B\text{-O}\rangle)$,[54] with small values of t ($t << 1$) indicating a large mismatch in the sizes of *A*- and *B*-cations, and thus predicting large magnitude tilting and twisting distortions. However, the situation for layered $A'AB_2O_7$ phases, such as $KNdM_2O_7$, is more complex because the tilting of the BO_6 units must accommodate both the size mismatch between *A*- and *B*-cations and the mismatch between *A*'- and *B*-cations.

The effect of the differing bonding requirements of the *A*- and *A*'-cations on the tilting distortions of layered perovskite phases can be seen in the evolution with *A*'-cation radius, of the ground-state structures of $A'NdNb_2O_7$ (*A*' = Group 1 metal) compounds shown in Figure 4. We can calculate the tolerance factor of the $NdNb_2O_7$ perovskite double sheets present in the $A'NdNb_2O_7$ phases using the ionic radii of the ions (Nd^{3+} = 1.27 Å, Nb^{5+} = 0.64 Å, O^{2-} = 1.40 Å) to yield a value of t = 0.925, indicating that in the absence of any *A*'-cation influence the $NdNb_2O_7$ sheets should exhibit large magnitude tilting and twisting distortions.

At room-temperature $CsNdNb_2O_7$ and $RbNdNb_2O_7$ adopt polar n = 2 Dion-Jacobson structures with relatively large magnitude $a^-a^-c^+$ and $a^-a^-c^+/\text{–}(a^-a^-c^+)$ tilting distortions respectively (Figure 4), consistent with the calculated tolerance factor of the $NdNb_2O_7$ sheets.[27, 55] However, as noted previously, while the $NdNb_2O_7$ sheets present in $CsNdNb_2O_7$ and $RbNdNb_2O_7$ are remarkably similar (same tilting pattern, same magnitude of tilt), the structures of the Cs and Rb compounds differ in the manner in which these distorted perovskite sheets are stacked – a difference which can be attributed to 'larger' Cs^+ and 'smaller' Rb^+ cations requiring subtly different structures to optimize the bonding requirements of the two different *A*'-cations and those of the formally 12-coordinate Nd^{3+} *A*-cations simultaneously.[27]

Exchanging the large Cs^+/Rb^+ cations for much smaller Na^+/Li^+ cations leads to a change from the (0, 0, z) sheet stacking of the Dion-Jacobson framework to the (½, ½, z) sheet stacking of the Ruddlesden-Popper framework, driven by the need to convert the 8-coordinate *A*'-cation sites in the Dion-Jacobson framework into 4-coordinate sites in the Ruddlesden-Popper framework to accommodate the much smaller Li^+ and Na^+ cations. $LiNdNb_2O_7$ adopts a polar n = 2 Ruddlesden-Popper structure with a relatively large magnitude $a^-a^-c^+/\text{–}(a^-a^-c^+)$ $NdNb_2O_7$ layer distortion (Figure 4), which can simultaneously satisfy the bonding requirements of the 4-coordinate Li^+ cations and the 12-coordinate Nd^{3+} cations, as illustrated by close to ideal BVS values (Li = 0.99, Nd = 3.07).[38] However, the larger ionic radius of Na^+ means this $LiNdNb_2O_7$ framework is unsuitable for $NaNdNb_2O_7$. Instead $NaNdNb_2O_7$ adopts a non-polar structure in which the $NdNb_2O_7$ sheets exhibit only a small magnitude $a^-b^0c^0/\ b^0a^-c^0$ tilting distortion (Figure 4).[38] The decrease in the degree of the distortion of the $NdNb_2O_7$ layers, compared to the analogous Cs, Rb and Li compounds, is motivated by the need to expand the 4-coordinate *A*'-cation sites to accommodate Na^+, however this inevitably means also expanding the 12-coordinate Nd^{3+} *A*-cation site weakening the bonding of this ion, highlighting the potential conflict between the need to optimize the bonding of both the *A*- and *A*'-cations simultaneously, and illustrating the role of the *A*'-cation in determining the type and magnitude of the $NdNb_2O_7$ layer tilting-distortion in $A'NdNb_2O_7$ phases.

In light of the examples provided by the other $A'NdNb_2O_7$ phases, the structure of $KNdNb_2O_7$ can also be seen as the result of a compromise between the bonding requirements of the *A*- and *A*'-cations. The intermediate ionic radius of K^+ drives the adoption of a (0, ½, z) stacking of the $NdNb_2O_7$ sheets, which leads to the formation of 6-coordinate trigonal prismatic *A*'-cation sites to accommodate the K^+ ions. The small magnitude $a^0b^+c^0/a^0$-b^+c^0 tilting distortion of the $NdNb_2O_7$ sheets in $KNdNb_2O_7$ (Figure 4) can be seen as the result of a need to expand the 6-coordinate *A*'-cations sites to accommodate K^+ cations, and again this also expands the 12-coordinate *A*-cation site compromising the bonding of the Nd^{3+} as illustrated by the non-optimal BVS values (Nd(1) = 2.894; Nd(2) 2.996). To further demonstrate the competition between *A*- and *A*'-cation bonding we have constructed a hypothetical structure in which the $a^-a^-c^+$ distorted $NdNb_2O_7$ layers from $CsNdNb_2O_7$ are stacked in a (0, ½, z) manner, as shown in Figure S8 in the Supporting Information. This hypothetical structure represents a situation where only the bonding requirements of the Nd^{3+} *A*-cations determine the type and magnitude of the $NdNb_2O_7$ layer distortion, as this framework has a close to ideal Nd^{3+} *A*-cation site (BVS = 3.06).[55] However, examination of the 4 different *A*'-cation sites in this framework, reveals they are far from ideal to accommodate K^+ with 2 being too small (BVS = 1.37, 1.41) and 2 being too large (BVS = 0.81, 0.85), consistent with the idea that the change in tilt pattern of the $NdNb_2O_7$ sheets from the large magnitude $a^-a^-c^+$ distortion of the Cs, Rb and Li phases, to the small magnitude $a^0b^+c^0/a^0$-b^+c^0 distortion observed in $KNdNb_2O_7$ occurs to better accommodate the K^+ cations. Together these features demonstrate that the *A*'-cations not only define the stacking pattern of the perovskite sheets (Cs, Rb = (0, 0, z); K = (0, ½, z); Na, Li = (½, ½, z)) but also have a large influence on the type and magnitude of the AB_2O_7 tilting distortions.

This is an important observation because the tilting distortions exhibited by $A'NdM_2O_7$ phases can have a decisive influence on the physical properties of these materials. For example, the polar (potentially ferroelectric) structures of $CsNdM_2O_7$,

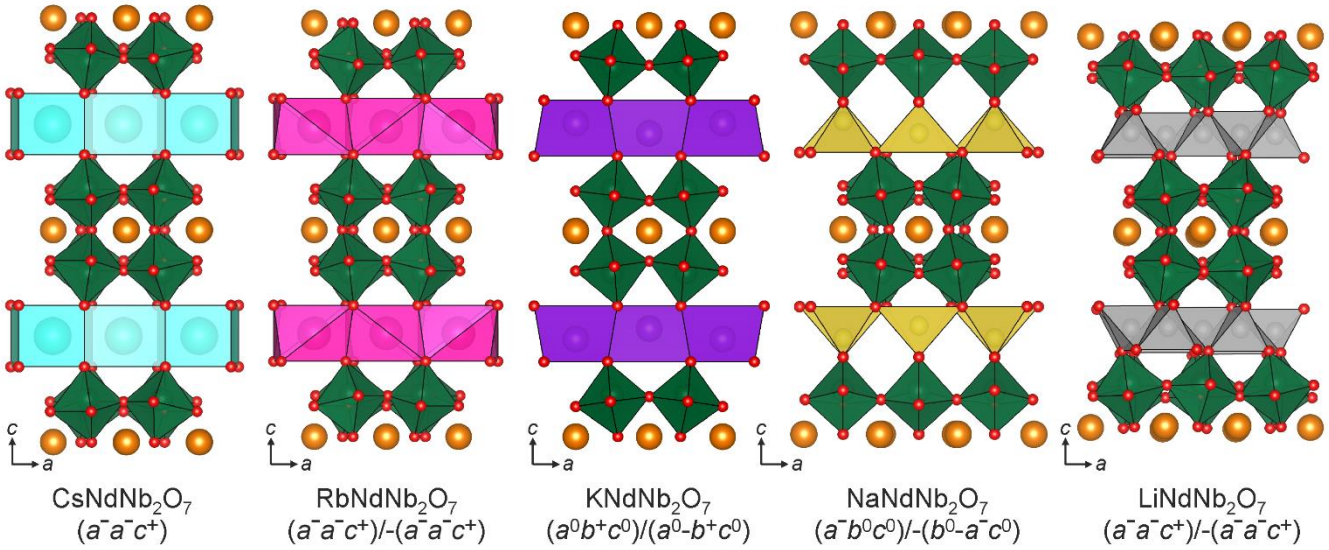

Figure 4. The crystal structures of the distorted, layered *A*'$NdNb_2O_7$ (*A*' = Group 1 metal) perovskite phases.

$RbNdM_2O_7$ and $LiNdM_2O_7$ arise via a trilinear coupling mechanism in which a combination of two tilting-distortion modes (e.g. the M_2^+ and M_5^- modes of $CsNdNb_2O_7$) break the inversion symmetry of the lattice and couple to a third polar distortion mode (e.g. the Γ_5^- mode of $CsNdNb_2O_7$) resulting in the observed polar structures. The observation that only a single tilting distortion mode (T_1^+) accompanies the Γ_4^- polar distortion mode in the $KNdM_2O_7$ phases rules out trilinear coupling as the origin of the polar structures of these phases. Instead it is likely that the Γ point polar distortions of the $KNdM_2O_7$ phases are driven by a second-order Jahn-Teller distortion of the NbO_6/TaO_6 units, as is commonly observed for octahedrally coordinated d^0 transition metal cations.

Analysis of the local NbO_6 and TaO_6 coordination polyhedra reveals that, as expected, the Nb/Ta cations are significantly displaced from the centers of the MO_6 units. The degree of off-centering can be quantified geometrically,[56] as described in detail in the supporting information, to yield values of $\Delta_d = 0.569$ and $\Delta_d = 0.709$ for $KNdTa_2O_7$ and $KNdNb_2O_7$ respectively. These values are larger than typically observed for $Ta^{5+}O_6$ (Δ_d =0.38) and $Nb^{5+}O_6$ (Δ_d =0.62), but follow the general trend that Nb > Ta. It should be noted that the majority of the off-centering of the M^{5+} cations is aligned along the *c*-axis, pointing 'out' of the NdM_2O_7 sheets, and as a result does not contribute to the polarization of the materials because pairs of MO_6 units are related by a mirror plane perpendicular to the *c*-axis. It is only the off-centering of the M^{5+} cations parallel to the *b*-axis which can contribute to the polarization of the materials, which can be measured as 0.074(5) Å and 0.089(3) Å for $KNdTa_2O_7$ and $KNdNb_2O_7$ respectively. As a result these materials could be considered as weakly canted antiferroelectrics.

Conclusion

Careful, sequential cation-exchange reactions have allowed us to unambiguously demonstrate that $KNdNb_2O_7$ and $KNdTa_2O_7$ adopt polar crystal structures in which the NCS arrangement of atoms is not stabilized by a trilinear coupled hybrid improper mechanism but is instead attributed to a SOJT mechanism. This contrasts with other members of the *A*'NdM_2O_7 series and suggests a competition between these two inversion-symmetry breaking mechanisms which can be tuned by the selection of the *A*'-cation.

ASSOCIATED CONTENT

Symmetry analysis of $n = 2$ (0, ½, *z*) layered perovskite phases; complete description of crystallographic analysis of $KNdNb_2O_7$ and $KNdTa_2O_7$; energy minimized structure of $KNdNb_2O_7$. This material is available free of charge via the Internet at http://pubs.acs.org.

AUTHOR INFORMATION

Corresponding Author

michael.hayward@chem.ox.ac.uk
nbenedek@cornell.edu

Author Contributions

The manuscript was written through contributions of all authors

ACKNOWLEDGMENT

Experiments at the Diamond Light Source were performed as part of the Block Allocation Group award "Oxford Solid State Chemistry BAG to probe composition-structure-property relationships in solids" (EE13284). Experiments at the ISIS pulsed neutron facility were supported by a beam time allocation from the STFC (RB1620305). SM thanks Somerville College for an Oxford Ryniker Lloyd scholarship. PSH and WZ thank the Welch Foundation (Grant E-1457) for support. NAB was supported by the National Science Foundation under award DMR-1550347. Computational resources were provided by the Cornell Center for Advanced Computing.

REFERENCES

1. Lines, M. E.; Glass, A. M., *Principles and Applications of Ferroelectrics and Related Materials*. Oxford University Press: Oxford, 1991.
2. Nye, F. J., *Physical Properties of Crystals*. Oxford University Press: Oxford, UK, 1957.
3. Halasyamani, P.; Poeppelmeier, K. R., Noncentrosymetric oxides. *Chem. Mater.* **1998,** *10*, 2753-2769.
4. Cohen, R. E., Origin of Ferroelectricity in Perovskite Oxides. *Nature* **1992,** *358* (6382), 136-138.

5. Kang, S. K.; Tang, H.; Albright, T. A., Structures for d^0 Ml_6 and Ml_5 Complexes. *J. Am. Chem. Soc.* **1993,** *115* (5), 1971-1981.

6. Kunz, M.; Brown, I. D., Out-of-Center Distortions around Octahedrally Coordinated d^0 Transition-Metals. *J. Solid State Chem.* **1995,** *115* (2), 395-406.

7. Pearson, R. G., The 2nd-Order Jahn-Teller Effect. *Theochem-Journal of Molecular Structure* **1983,** *12* (AUG), 25-34.

8. Lefebvre, I.; Lannoo, M.; Allan, G.; Ibanez, A.; Fourcade, J.; Jumas, J. C.; Beaurepaire, E., Electronic-Properties of Antimony Chalcogenides. *Phys. Rev. Lett.* **1987,** *59* (21), 2471-2474.

9. Lefebvre, I.; Szymanski, M. A.; Olivier-Fourcade, J.; Jumas, J. C., Electronic Structure of Tin Monochalcogenides from SnO to SnTe. *Phys. Rev. B* **1998,** *58* (4), 1896-1906.

10. Seshadri, R.; Hill, N. A., Visualizing the Role of Bi 6s "Lone Pairs" in the Off-Center Distortion in Ferromagnetic $BiMnO_3$. *Chem. Mater.* **2001,** *13* (9), 2892-2899.

11. Stoltzfus, M. W.; Woodward, P. M.; Seshadri, R.; Klepeis, J. H.; Bursten, B., Structure and Bonding in $SnWO_4$, $PbWO_4$, and $BiVO_4$: Lone Pairs vs Inert Pairs. *Inorg. Chem.* **2007,** *46* (10), 3839-3850.

12. Watson, G. W.; Parker, S. C., Origin of the Lone Pair of alpha-PbO from Density Functional Theory Calculations. *J. Phys. Chem. B* **1999,** *103* (8), 1258-1262.

13. Watson, G. W.; Parker, S. C.; Kresse, G., Ab Initio Calculation of the Origin of the Distortion of Alpha-PbO. *Phys. Rev. B* **1999,** *59* (13), 8481-8486.

14. Hill, N. A., Why Are There So Few Magnetic Ferroelectrics. *J. Phys. Chem. B* **2000,** *104*, 6694-6709.

15. Benedek, N. A.; Fennie, C. J., Hybrid Improper Ferroelectricity: A Mechanism for Controllable Polarization-Magnetization Coupling. *Phys. Rev. Lett.* **2011,** *106* (10), 107204.

16. Mulder, A. T.; Benedek, N. A.; Rondinelli, J. M.; Fennie, C. J., Turning ABO_3 Antiferroelectrics into Ferroelectrics: Design Rules for Practical Rotation-Driven Ferroelectricity in Double Perovskites and $A_3B_2O_7$ Ruddlesden-Popper Compounds. *Advanced Functional Materials* **2013,** *23* (38), 4810-4820.

17. Benedek, N. A.; Mulder, A. T.; Fennie, C. J., Polar octahedral rotations: A path to new multifunctional materials. *J. Solid State Chem.* **2012,** *195*, 11-20.

18. Rondinelli, J. M.; Fennie, C. J., Octahedral Rotation-Induced Ferroelectricity in Cation Ordered Perovskites. *Adv. Mater.* **2012,** *24* (15), 1961-1968.

19. Knapp, M. C.; Woodward, P. M., A-site Cation Ordering in $AA'BB'O_6$ Perovskites. *J. Solid State Chem.* **2006,** *179* (4), 1076-1085.

20. King, G.; Woodward, P. M., Cation Ordering in Perovskites. *J. Mater. Chem.* **2010,** *20*, 5785-5796.

21. Benedek, N. A.; Rondinelli, J. M.; Djani, H.; Ghosez, P.; Lightfoot, P., Understanding Ferroelectricity in Layered Perovskites: New Ideas and Insights From Theory and Experiments. *Dalton Trans.* **2015,** *44* (23), 10543-10558.

22. Oh, Y. S.; Luo, X.; Huang, F. T.; Wang, Y. Z.; Cheong, S. W., Experimental demonstration of hybrid improper ferroelectricity and the presence of abundant charged walls in $(Ca, Sr)_3Ti_2O_7$ crystals. *Nat. Mater.* **2015,** *14* (4), 407-413.

23. Yoshida, S.; Fujita, K.; Akamatsu, H.; Hernandez, O.; Sen Gupta, A.; Brown, F. G.; Padmanabhan, H.; Gibbs, A. S.; Kuge, T.; Tsuji, R.; Murai, S.; Rondinelli, J. M.; Gopalan, V.; Tanaka, K., Ferroelectric $Sr_3Zr_2O_7$: Competition between Hybrid Improper Ferroelectric and Antiferroelectric Mechanisms. *Advanced Functional Materials* **2018,** *28* (30), 1801856.

24. Yoshida, S.; Akamatsu, H.; Tsuji, R.; Hernandez, O.; Padmanabhan, H.; Sen Gupta, A.; Gibbs, A. S.; Mibu, K.; Murai, S.; Rondinelli, J. M.; Gopalan, V.; Tanaka, K.; Fujita, K., Hybrid Improper Ferroelectricity in $(Sr,Ca)_3Sn_2O_7$ and Beyond: Universal Relationship between Ferroelectric Transition Temperature and Tolerance Factor in *n*=2 Ruddlesden-Popper Phases. *J. Am. Chem. Soc.* **2018,** *140* (46), 15690-15700.

25. Liu, M. F.; Zhang, Y.; Lin, L. F.; Lin, L.; Yang, S. W.; Li, X.; Wang, Y.; Li, S. Z.; Yan, Z. B.; Wang, X. Z.; Li, X. G.; Dong, S.; Liu, J. M., Direct observation of ferroelectricity in $Ca_3Mn_2O_7$ and its prominent light absorption. *Appl. Phys. Lett.* **2018,** *113* (2), 022902.

26. Benedek, N. A., Origin of Ferroelectricity in a Family of Polar Oxides: The Dion-Jacobson Phases. *Inorg. Chem.* **2014,** *53* (7), 3769-3777.

27. Zhu, T.; Cohen, T.; Gibbs, A. S.; Zhang, W. G.; Halasyamani, P. S.; Hayward, M. A.; Benedek, N. A., Theory and Neutrons Combine To Reveal a Family of Layered Perovskites without Inversion Symmetry. *Chem. Mater.* **2017,** *29* (21), 9489-9497.

28. Zhu, T.; Gibbs, A. S.; Benedek, N. A.; Hayward, M. A., Complex Structural Phase Transitions of the Hybrid Improper Polar Dion-Jacobson Oxides RbNdM2O7 and CsNdM2O7 (M = Nb, Ta). *Chem. Mater.* **2020,** *32* (10), 4340-4346.

29. Schaak, R. E.; Mallouk, T. E., Perovskites by design: A toolbox of solid-state reactions. *Chem. Mater.* **2002,** *14* (4), 1455-1471.

30. Hayward, M. A., Soft chemistry synthesis of oxides. In *Comprehensive Inorganic Chemistry II*, Reedijk, J.; Poeppelmeier, K. R., Eds. Elsevier: Oxford, 2013; Vol. 2, pp 417-453.

31. Ranmohotti, K. G. S.; Josepha, E.; Choi, J.; Zhang, J. X.; Wiley, J. B., Topochemical Manipulation of Perovskites: Low-Temperature Reaction Strategies for Directing Structure and Properties. *Adv. Mater.* **2011,** *23* (4), 442-460.

32. Gopalakrishnan, J.; Bhat, V.; Raveau, B., $A^ILaNb_2O_7$ - a New Series of Layered Perovskites Exhibiting Ion-Exchange and Intercalation Behavior. *Mater. Res. Bull.* **1987,** *22* (3), 413-417.

33. Toda, K.; Sato, M., Synthesis and structure determination of new layered perovskite compounds, $ALaTa_2O_7$ and $ACa_2Ta_3O_{10}$ (A=Rb, Li). *J. Mater. Chem.* **1996,** *6* (6), 1067-1071.

34. Josepha, E. A.; Farooq, S.; Mitchell, C. M.; Wiley, J. B., Synthesis and thermal stability studies of a series of metastable Dion-Jacobson double-layered neodymium-niobate perovskites. *J. Solid State Chem.* **2014,** *216*, 85-90.

35. Sato, M.; Abo, J.; Jin, T., Structure examination of $NaLaNb_2O_7$ synthesized by soft chemistry. *Solid State Ionics* **1992,** *57* (3-4), 285-293.

36. Sato, M.; Abo, J.; Jin, T.; Ohta, M., Strucutre Determination of $KLaNb_2O_7$ Exhibiting Ion-Exchange Ability by X-ray Powder Diffraction. *Solid State Ionics* **1992,** *51* (1-2), 85-89.

37. Sato, M.; Abo, J.; Jin, T.; Ohta, M., Strucutre and Ionic Conductivity of $MLaNb_2O_7$ (M = K, Na, Li, H). *J. Alloys Compounds* **1993,** *192* (1-2), 81-83.

38. Zhu, T.; Khalsa, G.; Havas, D. M.; Gibbs, A. S.; Zhang, W.; Halasyamani, P. S.; Benedek, N. A.; Hayward, M. A., Cation Exchange as a Mechanism To Engineer Polarity in Layered Perovskites. *Chem. Mater.* **2018,** *30*, 8915-8924.

39. Larson, A. C.; Von Dreele, R. B. *General Structure Analysis System*, Los Alamos National Laboratory Report LAUR 86-748: 2000.

40. Ok, K. M.; Chi, E. O.; Halasyamani, P. S., Bulk characterization methods for non-centrosymmetric materials: second-harmonic generation, piezoelectricity, pyroelectricity, and ferroelectricity. *Chem. Soc. Rev.* **2006,** *35*, 710-717.

41. Kresse, G.; Hafner, J., Ab-initio molecular-dynamics for liquid-metals. *Phys. Rev. B* **1993,** *47* (1), 558-561.

42. Kresse, G.; Hafner, J., Ab-initio Molecular Dynamics Simulation of the Liquid-metal Amorphous-semiconductor Transition in Germanium. *Phys. Rev. B* **1994,** *49* (20), 14251-14269.

43. Kresse, G.; Furthmuller, J., Efficiency of ab-initio total energy calculations for metals and semiconductors using a plane-wave basis set. *Comput. Mater. Sci.* **1996,** *6* (1), 15-50.

44. Kresse, G.; Furthmuller, J., Efficient iterative schemes for ab initio total-energy calculations using a plane-wave basis set. *Phys. Rev. B* **1996,** *54* (16), 11169-11186.

45. Perdew, J. P.; Ruzsinszky, A.; Csonka, G. I.; Vydrov, O. A.; Scuseria, G. E.; Constantin, L. A.; Zhou, X. L.; Burke, K., Restoring the density-gradient expansion for exchange in solids and surfaces. *Phys. Rev. Lett.* **2008,** *100* (13), 136406.

46. Blochl, P. E., Projector augmented-wave method. *Phys. Rev. B* **1994,** *50* (24), 17953-17979.

47. Kresse, G.; Joubert, D., From ultrasoft pseudopotentials to the projector augmented-wave method. *Phys. Rev. B* **1999,** *59* (3), 1758-1775.

48. Stokes, H. T.; Hatch, D. M.; Campbell, B. J. *ISOTROPY Software Suite*, iso.byu.edu, 2007.

49. Aroyo, M. I.; Kirov, A.; Capillas, C.; Perez-Mato, J. M.; Wondratschek, H., Bilbao crystallographic server. II. Representations

of crystallographic point groups and space groups. *Acta Cryst. Sect. A: Found. Crystallogr.* **2006,** *62*, 115-128.

50. Aroyo, M. I.; Perez-Mato, J. M.; Capillas, C.; Kroumova, E.; Ivantchev, S.; Madariaga, G.; Kirov, A.; Wondratschek, H., Bilbao crystallographic server: I. Databases and crystallographic computing programs. *Z. Kristallogr. - Cryst. Mater.* **2006,** *221* (1), 15-27.

51. Campbell, B. J.; Stokes, H. T.; Tanner, D. E.; Hatch, D. M., ISODISPLACE: a web-based tool for exploring structural distortions. *J. Appl. Crystallogr.* **2006,** *39*, 607-614.

52. Glazer, A. M., Classification of tilted Octahedra in Perovskites. *Acta Crystallogr. Sect. B-Struct. Commun.* **1972,** *B 28* (NOV15), 3384-3392.

53. Woodward, P. M., Octahedral tilting in perovskites .1. Geometrical considerations. *Acta Crystallogr. Sect. B-Struct. Commun.* **1997,** *53*, 32-43.

54. Goldschmidt, V. M., Die Gesetze der Krystallochemie. *Naturwissenschaften* **1926,** *14*, 477-485.

55. Snedden, A.; Knight, K. S.; Lightfoot, P., Structural distortions in the layered perovskites $CsANb_2O_7$ (A = Nd, Bi). *J. Solid State Chem.* **2003,** *173* (2), 309-313.

56. Halasyamani, P., Asymmetric Cation Coordination in Oxide Materials: Influence of Lone-Pair Cations on the Intra-octahedral Distortion in d^0 Transition Metals. *Chem. Mater.* **2004,** *16*, 3586-3592.

SYNOPSIS TOC